

# Modelling redshift space distortions in hierarchical cosmologies

E. Jennings<sup>1,2\*</sup>, C. M. Baugh<sup>1</sup>, S. Pascoli<sup>2</sup>

<sup>1</sup> *Institute for Computational Cosmology, Department of Physics, Durham University, South Road, Durham, DH1 3LE, U.K.*

<sup>2</sup> *Institute for Particle Physics Phenomenology, Department of Physics, Durham University, South Road, Durham, DH1 3LE, U.K.*

## ABSTRACT

The anisotropy of clustering in redshift space provides a direct measure of the growth rate of large scale structure in the Universe. Future galaxy redshift surveys will make high precision measurements of these distortions, and will potentially allow us to distinguish between different scenarios for the accelerating expansion of the Universe. Accurate predictions are needed in order to distinguish between competing cosmological models. We study the distortions in the redshift space power spectrum in  $\Lambda$ CDM and quintessence dark energy models, using large volume N-body simulations, and test predictions for the form of the redshift space distortions. We find that the linear perturbation theory prediction by Kaiser (1987) is a poor fit to the measured distortions, even on surprisingly large scales  $k \geq 0.05h\text{Mpc}^{-1}$ . An improved model for the redshift space power spectrum, including the non-linear velocity divergence power spectrum, is presented and agrees with the power spectra measured from the simulations up to  $k \sim 0.2h\text{Mpc}^{-1}$ . We have found a density-velocity relation which is cosmology independent and which relates the non-linear velocity divergence spectrum to the non-linear matter power spectrum. We provide a formula which generates the non-linear velocity divergence  $P(k)$  at any redshift, using only the non-linear matter power spectrum and the linear growth factor at the desired redshift. This formula is accurate to better than 5% on scales  $k < 0.2h\text{Mpc}^{-1}$  for all the cosmological models discussed in this paper. Our results will extend the statistical power of future galaxy surveys.

**Key words:** Methods: Numerical - Cosmology: theory - large-scale structure of the Universe

## 1 INTRODUCTION

The rate at which cosmic structures grow is set by a competition between gravitational instability and the rate of expansion of the Universe. The growth of structure can be measured by analysing the distortions in the galaxy clustering pattern, when viewed in redshift space (i.e. when a galaxy's redshift is used to infer its radial position). Proof of concept of this approach came recently from Guzzo et al. (2008) who used spectroscopic data for 10,000 galaxies from the VIMOS-VLT Deep Survey (Le Fevre et al. 2005) to measure the growth rate of structure at redshift  $z = 0.77$  to an accuracy of  $\sim 40\%$  (see also Peacock et al. 2001). To distinguish between competing explanations for the accelerating expansion of the Universe, we need to measure the growth of structure to an accuracy of a few percent over a wide redshift interval. The next generation of galaxy redshift surveys, such

as ESA's Euclid mission (Cimatti et al. 2009), will be able to achieve this precision. These redshift space distortions are commonly modelled using a linear perturbation theory expression. We test the validity of this approximation using large volume N-body simulations to model the redshift space distortions in  $\Lambda$ CDM and quintessence dark energy models, to see if it works at the level required to take advantage of the information in forthcoming surveys. The large volume of our simulations means that we are able to find the limits of perturbation theory models. We can also study the impact of non-linearities on large scales in cosmologies with different expansion histories from  $\Lambda$ CDM, such as quintessence dark energy.

One explanation of the accelerating expansion of the Universe is that a negative pressure dark energy component makes up approximately 70% of the present density of the Universe (Komatsu et al. 2009; Sánchez et al. 2009). Examples of dark energy models include the cosmological constant and a dynamical scalar field such as quintessence (see e.g.

\* E-mail: elise.jennings@durham.ac.uk

Copeland et al. 2006, for a review). Other possible solutions require modifications to general relativity and include extensions to the Einstein-Hilbert action, such as  $f(R)$  theories or braneworld cosmologies (see e.g. Dvali et al. 2000; Oyaizu 2008).

The expansion history of the Universe is described by the scale factor,  $a(t)$ . Dark energy and modified gravity models can produce similar expansion histories for the Universe, which can be derived from the Hubble parameter measured, for example, using type Ia supernovae. As both dark energy and modified gravity models can be described using an effective equation of state which specifies the expansion history, it is not possible to distinguish between these two possibilities using measurements of the expansion history alone.

The growth rate is a measure of how rapidly structures are forming in the Universe. Dark energy or modified gravity models predict different growth rates for the large scale structure of the Universe, which can be measured using redshift space distortions of clustering. As noted by Linder (2005), in the case of general relativity, the second order differential equation for the growth of density perturbations depends only on the expansion history through the Hubble parameter,  $H(a)$ , or the equation of state,  $w(a)$ . This is not the case for modified gravity theories. By comparing the cosmic expansion history with the growth of structure, it is possible to distinguish the physical origin of the accelerating expansion of the Universe as being due either to dark energy or modified gravity (Lue, Scoccimarro & Starkman 2004; Linder 2005). If there is no discrepancy between the observed growth rate and the theoretical prediction assuming general relativity, this implies that a dark energy component alone can explain the accelerated expansion.

Galaxy redshift surveys allow us to study the 3D spatial distribution of galaxies and clusters. In a homogeneous universe, redshift measurements would probe only the Hubble flow and would provide accurate radial distances for galaxies. In reality, peculiar velocities are gravitationally induced by inhomogeneous structure and distort the measured distances. Kaiser (1987) described the anisotropy of the clustering pattern in redshift space but restricted his calculation to large scales where linear perturbation theory should be applicable. In the linear regime, the matter power spectrum in redshift space is a function of the power spectrum in real space and the parameter  $\beta = f/b$  where  $f$  is the linear growth rate. The linear bias factor,  $b$ , characterises the clustering of galaxies with respect to the underlying mass distribution (e.g. Kaiser 1987). Scoccimarro (2004) extended the analysis of Kaiser (1987) into the non-linear regime, including the contribution of peculiar velocities on small scales. We test this model in this paper.

Perturbations in bulk flows converge more slowly than perturbations in density, and so very large volume simulations are needed to model these flows, and hence the redshift space distortion of clustering, accurately. Our simulation boxes are 125 times the volume of those used by Cole et al. (1994) and  $\sim 30$  times the volume of the N-body results interpreted by Scoccimarro (2004). Percival & White (2009) used a single  $1h^{-1}\text{Gpc}$  box to study redshift space distortions in a  $\Lambda\text{CDM}$  model. Their simulation is over three times smaller than the one we consider.

This paper is organised as follows: In Section 2 we discuss the linear growth rate and review the theory of redshift

space distortions on linear and non-linear scales. In Section 3 we present the quintessence models considered and the details of our N-body simulations. The main results of the paper are presented in Sections 4 and 5. The linear theory redshift space distortion, as well as models for the redshift space power spectrum which include non-linear effects are examined in Section 4 for various dark energy cosmologies. In Section 5 we present the density-velocity relation measured from the simulations. Using this relation the non-linear models used in the previous section can be made cosmology independent. We present a prescription for obtaining the non-linear velocity divergence power spectrum from the non-linear matter power spectrum at an arbitrary redshift in Section 5.2. Our conclusions are presented in Section 6.

## 2 REDSHIFT SPACE DISTORTIONS

In Section 2.1 we consider several parametrizations which are commonly used for the linear growth rate. In Section 2.2 we review linear perturbation theory for redshift space distortions and discuss the assumptions that are used in this approach. In Section 2.3 we present several models proposed to describe the distortions in the non-linear regime. A similar review can be found in Percival & White (2009).

### 2.1 Linear growth rate as a probe of gravity

The linear growth rate is a promising probe of the nature of dark energy (Guzzo et al. 2008; Wang 2008; Linder 2008; Song & Percival 2009; White et al. 2009; Percival & White 2009; Stril et al. 2010; Simpson & Peacock 2010). Although the growth equation for dark matter perturbations is easy to solve exactly, it is common to consider parametrizations for the linear growth rate,  $f = d\ln D/d\ln a$ , where  $D(a)$  is the linear growth factor. These parametrizations employ different variables with distinct dependencies on the expansion and growth histories.

A widely used approximation for  $f$ , first suggested by Peebles (1976), is  $f(z) \approx \Omega_m^{0.6}$ . Lahav et al. (1991) found an expression for  $f$ , in terms of the present day densities of matter,  $\Omega_m$ , and dark energy,  $\Omega_{DE}$ , which showed only a weak dependence on the dark energy density, with  $f \approx \Omega_m^{0.6} + \Omega_{DE}/70 (1 + \Omega_m/2)$ . Linder (2005) extended the analysis of Wang & Steinhardt (1998) to find a new fitting formula to the exact solution for the growth factor, which he cast in the following form

$$g(a) = \frac{D(a)}{a} \approx \exp \left( \int_0^a d\ln a [\Omega_m^\gamma(a) - 1] \right), \quad (1)$$

where  $\gamma$  is the index which parametrises the growth history, while the expansion history is described by the matter density  $\Omega_m(a)$ . Linder (2005) proposed the empirical result  $\gamma = 0.55 + 0.05[1 + w(z=1)]$ , where  $w$  is the dark energy equation of state, which gives  $f = \Omega_m^{0.55}$  for a cosmological constant (see also Linder & Cahn 2007). We discuss this formula for  $f$  further in Section 3 when we introduce the quintessence dark energy models used in this paper.

## 2.2 Linear redshift space distortions

The comoving distance to a galaxy,  $\vec{s}$ , differs from its true distance,  $\vec{x}$ , due to its peculiar velocity,  $\vec{v}(\vec{x})$  (i.e. an additional velocity to the Hubble flow), as

$$s = x + \frac{\vec{v} \cdot \hat{x}}{H(a)}, \quad (2)$$

where  $H(a)$  is the Hubble parameter and  $\vec{v} \cdot \hat{x}$  is the peculiar velocity along the line of sight. Inhomogeneous structure in the universe induces peculiar motions which distorts the clustering pattern measured in redshift space on all scales. This effect must be taken into account when analyzing three dimensional datasets which use redshift as the radial coordinate. Redshift space effects alter the appearance of the clustering of matter, and together with non-linear evolution and bias, lead the power spectrum to depart from simple linear perturbation theory predictions.

On small scales, randomised velocities associated with virialised structures decrease the power. The dense central regions of galaxy clusters look elongated along the line of sight in redshift space, which produces ‘fingers of God’ (Jackson 1972) in redshift survey cone plots. On large scales, coherent bulk flows distort clustering statistics, (see Hamilton 1998, for a review of redshift space distortions). For growing perturbations on large scales, the overall effect of redshift space distortions is to enhance the clustering amplitude. Any difference in the velocity field due to mass flowing from underdense regions to high density regions will alter the volume element, causing an enhancement of the apparent density contrast in redshift space,  $\delta_s(\vec{r})$ , compared to that in real space,  $\delta_r(\vec{r})$ . This effect was first analyzed by Kaiser (1987) and can be approximated by

$$\delta_s(r) = \delta_r(r)(1 + \mu^2 \beta), \quad (3)$$

where  $\mu$  is the cosine of the angle between the wavevector,  $\vec{k}$ , and the line of sight,  $\beta = f/b$  and the bias,  $b = 1$  for dark matter.

The Kaiser formula (Eq. 3) relates the overdensity in redshift space to the corresponding value in real space using several approximations:

1. The small scale velocity dispersion can be neglected.
2. The velocity gradient  $|\mathrm{d}\vec{u}/\mathrm{d}\mathbf{r}| \ll 1$ .
3. The velocity and density perturbations satisfy the linear continuity equation.
4. The real space density perturbation is assumed to be small,  $|\delta(r)| \ll 1$ , so that higher order terms can be neglected.

All of these assumptions are valid on scales that are well within the linear regime and will break down on different scales as the density fluctuations grow. The linear regime is therefore defined over a different range of scales for each effect.

The matter power spectrum in redshift space can be decomposed into multipole moments using Legendre polynomials,  $L_l(\mu)$ ,

$$P(k, \mu) = \sum_{l=0}^{2l} P_l(k) L_l(\mu). \quad (4)$$

The anisotropy in  $P(\vec{k})$  is symmetric in  $\mu$ , as  $P(k, \mu) = P(k, -\mu)$ , so only even values of  $l$  are summed over. Each

multipole moment is given by

$$P_l^s(k) = \frac{2l+1}{2} \int_{-1}^1 P(k, \mu) L_l(\mu) \mathrm{d}\mu, \quad (5)$$

where the first two non-zero moments have Legendre polynomials,  $L_0(\mu) = 1$  and  $L_2(\mu) = (3\mu^2 - 1)/2$ . Using the redshift space density contrast, Eq. 3 can be used to form  $P(k, \mu)$  and then integrating over the cosine of the angle  $\mu$  gives the spherically averaged monopole power spectrum in redshift space,  $P_0^s(k)$ ,

$$\frac{P_0^s(k)}{P^r(k)} = 1 + \frac{2}{3}f + \frac{1}{5}f^2, \quad (6)$$

where  $P^r(k)$  denotes the matter power spectrum in real space. In practice,  $P^r(k)$  cannot be obtained directly for a real survey without making approximations (e.g. Baugh & Efstathiou 1994).

In this paper we also consider the estimator for  $f$  suggested by Cole et al. (1994), which is the ratio of quadrupole to monopole moments of the redshift space power spectrum,  $P_2^s(k)/P_0^s(k)$ . From Eq. 3 and after spherically averaging, the estimator for  $f$  is then

$$\frac{P_2^s(k)}{P_0^s(k)} = \frac{4f/3 + 4f^2/7}{1 + 2f/3 + f^2/5}, \quad (7)$$

which is independent of the real space power spectrum. Here, as before,  $f = \beta/b$ , with  $b = 1$  for dark matter.

## 2.3 Modelling non-linear distortions to the power spectrum in redshift space

Assuming the line of sight component is along the  $z$ -axis, the fully non-linear relation between the real and redshift space power spectrum can be written as (Scoccimarro et al. 1999)

$$P^s(k, \mu) = \int \frac{\mathrm{d}^3\mathbf{r}}{(2\pi)^3} e^{-i\mathbf{k} \cdot \mathbf{r}} \langle e^{i\lambda \Delta u_z} [\delta(\mathbf{x}) - f \nabla_z \cdot u_z(\mathbf{x})] \times [\delta(\mathbf{x}') - f \nabla'_z \cdot u_z(\mathbf{x}')] \rangle, \quad (8)$$

where  $\lambda = fk\mu$ ,  $u_z$  is the comoving peculiar velocity along the line of sight,  $\Delta u_z = u_z(\mathbf{x}) - u_z(\mathbf{x}')$ ,  $\mathbf{r} = \mathbf{x} - \mathbf{x}'$  and the only approximation made is the plane parallel approximation. This expression is the Fourier analog of the ‘streaming model’ first suggested by Peebles (1980) and modified by Fisher (1995) to take into account the density-velocity coupling. At small scales (as  $k$  increases) the exponential component damps the power, representing the impact of randomised velocities inside gravitationally bound structures.

Simplified models for redshift space distortions are frequently used. Examples include multiplying Eq. 6 by a factor which attempts to take into account small scale effects and is either a Gaussian or an exponential (Peacock & Dodds 1994). A popular phenomenological example of this which incorporates the damping effect of velocity dispersion on small scales is the so called ‘dispersion model’ (Peacock & Dodds 1994),

$$P^s(k, \mu) = P^r(k)(1 + \beta\mu^2)^2 \frac{1}{(1 + k^2\mu^2\sigma_p^2/2)}, \quad (9)$$

where  $\sigma_p$  is the pairwise velocity dispersion along the line of sight, which is treated as a parameter to be fitted to the

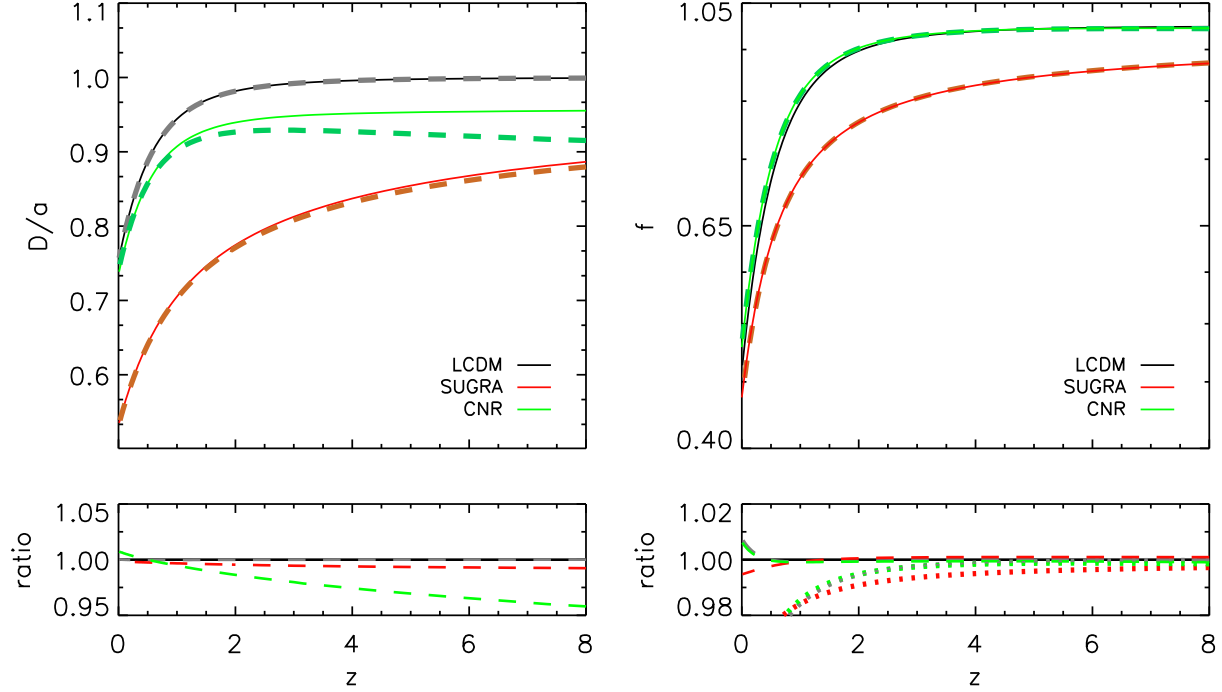


**Figure 1.** Left panel: The linear growth factor divided by the scale factor as a function of redshift for the SUGRA and CNR quintessence models and  $\Lambda$ CDM, as indicated by the key. Right panel: The linear growth rate,  $f = d\ln D/d\ln a$ , for the two dark energy models and  $\Lambda$ CDM as a function of redshift. In both the left and right main panels, solid lines represent the exact solution for the linear growth factor and growth rate and dashed lines show the fitting formula given in Eq. 1. Note in the right main panel the  $\Lambda$ CDM grey dashed line has been omitted for clarity. The lower left hand panel shows the formula for  $D(a)/a$  given by Linder (2005) divided by the exact solution as a function of redshift. The ratio of the formula in Eq. 1 for the growth rate,  $f$ , to the exact solution is shown in the lower right hand panel. Also in the lower right panel the dotted lines show the ratio of the fitting formula  $f = \Omega_m^{0.6}$  to the exact solution for each of the dark energy models plotted as a function of redshift.

data. Using numerical simulations, Hatton & Cole (1999) found a fit to the quadrupole to monopole ratio  $P_2^s/P_0^s = (P_2^s/P_0^s)_{\text{lin}}(1 - x^{1.22})$  to mimic damping and non-linear effects, where  $(P_2^s/P_0^s)_{\text{lin}}$  is the linear theory prediction given by Eq. 7,  $x = k/k_1$  and  $k_1$  is a free parameter. They extended the dynamic range of simulations, to replicate the effect of a larger box, using the approximate method for adding long wavelength power suggested by Cole (1997).

The velocity divergence auto power spectrum is the ensemble average,  $P_{\theta\theta} = \langle |\theta|^2 \rangle$  where  $\theta = \vec{\nabla} \cdot \vec{u}$  is the velocity divergence. The cross power spectrum of the velocity divergence and matter density is  $P_{\delta\theta} = \langle |\delta\theta| \rangle$ , where in this notation the matter density auto spectrum is  $P_{\delta\delta} = \langle |\delta|^2 \rangle$ . In Eq. 8, the term in square brackets can be re-written in terms of these non-linear velocity divergence power spectra by multiplying out the brackets and using the fact that  $\mu_i = \vec{k}_i \cdot \vec{z}/k_i$ . Scoccimarro (2004) proposed the following model for the redshift space power spectrum in terms of  $P_{\delta\delta}$ , the non-linear matter power spectrum,  $P_{\theta\theta}$  and  $P_{\delta\theta}$ ,

$$P^s(k, \mu) = (P_{\delta\delta}(k) + 2f\mu^2 P_{\delta\theta}(k) + f^2\mu^4 P_{\theta\theta}(k)) \times e^{-(fk\mu\sigma_v)^2}, \quad (10)$$

where  $\sigma_v$  is the 1D linear velocity dispersion given by

$$\sigma_v^2 = \frac{1}{3} \int \frac{P_{\theta\theta}(k)}{k^2} d^3k. \quad (11)$$

In linear theory,  $P_{\theta\theta}$  and  $P_{\delta\theta}$  take the same form as  $P_{\delta\delta}$  and depart from this at different scales. Using a simulation with

$512^3$  particles in a box of length  $479h^{-1}\text{Mpc}$  (Yoshida et al. 2001), Scoccimarro (2004) showed that this simple ansatz for  $P_s(k, \mu)$  was an improvement over the Kaiser formula when comparing to N-body simulations in a  $\Lambda$ CDM cosmology. As this is a much smaller simulation volume than the one we use to investigate redshift space distortions we are able to test the fit to the measured power spectrum on much larger scales and to higher accuracy.

### 3 N-BODY SIMULATIONS OF DARK ENERGY

In the following sections we briefly review the quintessence models discussed in this paper and the N-body simulations used to measure various power spectra.

#### 3.1 Quintessence models

In quintessence models of dark energy, the cosmological constant is replaced by an extremely light scalar field which evolves slowly (Ratra & Peebles 1988; Wetterich 1988; Caldwell et al. 1998; Ferreira & Joyce 1998). Different quintessence dark energy models have different dark energy densities as a function of time,  $\Omega_{\text{DE}}(z)$ . This implies a different growth history for dark matter perturbations from that expected in  $\Lambda$ CDM. In this paper we consider three quintessence models, each with a different evolution for the dark energy equation of state parameter,  $w(a)$ .

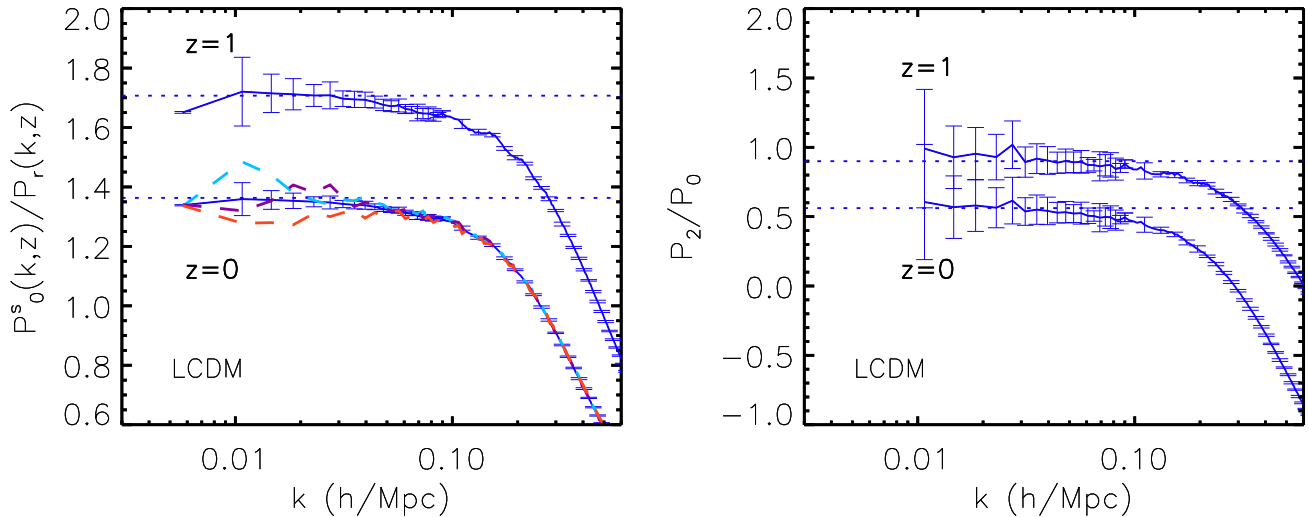


**Figure 2.** Left panel: The ratio of the monopole redshift power spectra and real space power spectra measured from the  $\Lambda$ CDM simulation at  $z = 0$  and  $z = 1$  are plotted as blue lines. The error bars plotted represent the scatter between the different power spectra from four  $\Lambda$ CDM simulations set up with different realisations of the density field with the distortions imposed along either the  $x$ ,  $y$  or  $z$  axis and averaged. The power spectra  $P(k, \mu = k_x/k)$ ,  $P(k, \mu = k_y/k)$  and  $P(k, \mu = k_z/k)$  measured from one simulation are plotted as the cyan, purple and red dashed lines respectively. Right panel: The ratio of the quadrupole to monopole moment of the redshift space power spectrum measured from the simulations at  $z = 0$  and  $z = 1$  in  $\Lambda$ CDM are plotted in blue. It was not possible to accurately measure the quadrupole to monopole power in the first bin, so this point has not been plotted in the right hand panel. Note for wavenumbers  $k > 0.1 h\text{Mpc}^{-1}$ , only every fifth error bar is plotted for clarity. The Kaiser formula, given by Eq. 6, is plotted as a blue dotted line. The error bars were obtained as described for the left-hand panel.

These models are a representative sample of a range of quintessence models and are a subset of those considered by Jennings et al. (2010) to which we refer the reader for further details. Briefly, the SUGRA model of Brax & Martin (1999) has an equation of state today of  $w_0 = -0.82$  and a linear growth factor which differs from  $\Lambda$ CDM by 20% at  $z = 5$ . The 2EXP model has an equation of state that makes a rapid transition to  $w_0 = -1$  at  $z = 4$  and since then has a similar expansion history to  $\Lambda$ CDM (Barreiro et al. 2000). The CNR quintessence model has a non-negligible amount of dark energy at early times and an equation of state today of  $w_0 = -1$  (Copeland et al. 2000). The dark energy equation of state for each model is described using a 4 variable parametrization for  $w(a)$  which is able to accurately describe the expansion history over the full range of redshifts modelled by the simulations (Corasaniti & Copeland 2003).

The presence of small but appreciable amounts of dark energy at early times also modifies the growth rate of fluctuations from that expected in a matter dominated universe and hence changes the shape of the linear theory  $P(k)$  from the  $\Lambda$ CDM prediction (Jennings et al. 2010). The CNR quintessence model used in this paper has non-negligible amounts of dark energy at high redshifts and so could be classed as an ‘early dark energy’ model (Doran & Robbers 2006). As a result, the linear theory power spectrum is appreciably different from that in a  $\Lambda$ CDM cosmology, with a broader turnover, (see Jennings et al. 2010, for further details).

Quintessence dark energy models will not necessarily agree with observational data if we adopt the same cosmological parameters as used in the best fitting  $\Lambda$ CDM cosmology. These best fit parameters were found using the observational constraints on distances such as the angular di-

**Table 1.** Cosmological parameters used in the simulations. The first column gives the cosmological model, the second the present day matter density,  $\Omega_m$ , the third the baryon density,  $\Omega_b$  and the fourth the Hubble constant,  $h$ , in units of  $100 \text{ km s}^{-1} \text{ Mpc}^{-1}$ .

Model	$\Omega_m$	$\Omega_b$	$h$
$\Lambda$ CDM / 2EXP	0.26	0.044	0.715
SUGRA	0.24	0.058	0.676
CNR	0.28	0.042	0.701

ameter distance to last scattering and the sound horizon at this epoch, from the cosmic microwave background, as well as distance measurements from the baryonic acoustic oscillations and Type Ia supernovae (Jennings et al. 2010). In this paper the best fitting cosmological parameters for each quintessence model are used in the N-body simulations, as listed in Table 1.

In the left panel of Fig. 1, we plot the exact solution for the linear theory growth factor, divided by the scale factor, as a function of redshift together with the fitting formula in Eq. 1. The 2EXP quintessence model is not plotted in Fig. 1 as the linear growth factor for this model differs from  $\Lambda$ CDM only at high redshifts,  $z > 10$ . Linder (2005) found that the formula in Eq. 1 reproduces the growth factor to better than 0.05% for  $\Lambda$ CDM cosmologies and to  $\sim 0.25\%$  for different dynamical quintessence models to the ones considered in this paper. We have verified that this fitting formula for  $D$  is accurate to  $\sim 1\%$  for the SUGRA and 2EXP dark energy models used in this paper, over a range of redshifts. Note, in cosmological models which feature non negligible amounts of dark energy at high redshifts, a further correction factor is needed to this parametrisation (Linder 2009). Using the parametrization for  $w(a)$  provided by Doran & Robbers

(2006) for ‘early dark energy’, Linder (2009) proposed a single correction factor which was independent of redshift. The CNR model has a high fractional dark energy density at early times and as a result we do not expect the linear theory growth to be accurately reproduced by Eq. 1. As can be seen in Fig. 1 for the CNR model, any correction factor between the fitting formula suggested by Linder (2005) and the exact solution for  $D/a$  would depend on redshift and is not simply a constant. In this case, the ‘early dark energy’ parametrisation of Doran & Robbers (2006) is not accurate enough to fully describe the dynamics of the CNR quintessence model. This difference is  $\sim 5\%$  at  $z = 8$  for the CNR model, as can be seen in the ratio plot in the left panel of Fig 1. The exact solution for the linear growth rate,  $f$ , and the fitting formula in Eq. 1,  $f = \Omega_m^{\gamma}(a)$ , is plotted in the right panel of Fig. 1. The old approximation  $f = \Omega_m^{0.6}$ , is plotted in the bottom right panel in Fig. 1. The dotted lines represent the ratio  $f = \Omega_m^{0.6}$  to the exact solution for each of the dark energy models. It is clear that this approximation for the growth factor is not as accurate as the formula in Eq. 1 over the same range of redshifts.

### 3.2 Simulation Details

We use the N-body simulations carried out by Jennings et al. (2010). These simulations were performed at the Institute of Computational Cosmology using a memory efficient version of the TreePM code GADGET-2, called L-GADGET-2 (Springel 2005). For the  $\Lambda$ CDM model we used the following cosmological parameters:  $\Omega_m = 0.26$ ,  $\Omega_{DE} = 0.74$ ,  $\Omega_b = 0.044$ ,  $h = 0.715$  and a spectral tilt of  $n_s = 0.96$  (Sánchez et al. 2009). The linear theory rms fluctuation in spheres of radius  $8 h^{-1}$  Mpc is set to be  $\sigma_8 = 0.8$ . For each of the quintessence models, a four variable parametrization of the dark energy equation of state is used as described above. In each case, the cosmological parameters used are the best fitting parameters to observational constraints from the cosmic microwave background, baryonic acoustic oscillations and supernovae Ia taking into account the impact of the quintessence model. (Stage III in the terminology of Jennings et al. 2010).

The simulations use  $N = 646^3 \sim 269 \times 10^6$  particles to represent the matter distribution in a computational box of comoving length  $1500 h^{-1}$  Mpc. The comoving softening length is  $50 h^{-1}$  kpc. The particle mass in the  $\Lambda$ CDM simulation is  $9.02 \times 10^{11} h^{-1} M_{\odot}$  and is slightly different in the other runs due to changes in  $\Omega_m$  (see Table 1). The initial conditions were set up starting from a glass configuration of particles (White 1994; Baugh et al. 1995). In order to limit the impact of the initial displacement scheme we chose a starting redshift of  $z = 200$ .

The linear theory power spectrum used to generate the initial conditions was obtained using CAMB (Lewis & Bridle 2002). We use a modified version of CAMB which incorporates the influence of dark energy on dark matter clustering at early times (Fang et al. 2008).

In each model the power spectrum at redshift zero is normalised to have  $\sigma_8 = 0.8$ . Using the linear growth factor for each dark energy model, the linear theory  $P(k)$  was then evolved backwards to the starting redshift of  $z = 200$  in order to generate the initial conditions. The power spectrum was computed by assigning the particles

to a mesh using the cloud in cell (CIC) assignment scheme (Hockney & Eastwood 1981) and performing a fast Fourier transform (FFT) of the density field. To compensate for the mass assignment scheme we perform an approximate deconvolution following Baumgart & Fry (1991).

## 4 RESULTS I: THE MATTER POWER SPECTRUM IN REAL AND REDSHIFT SPACE

In Sections 4.1 and 4.2 we present the redshift space distortions measured from the simulations in  $\Lambda$ CDM and quintessence cosmologies, and we compare with the predictions of the linear and non-linear models discussed in Section 2.3.

### 4.1 Testing the linear theory redshift space distortion

In the left panel of Fig. 2, we plot the ratio of the redshift space to real space power spectra, measured from the  $\Lambda$ CDM simulation at  $z = 0$  and  $z = 1$ . Using the plane parallel approximation, we assume the observer is at infinity and as a result the velocity distortions are imposed along one direction in  $k$ -space. If we choose the line of sight direction to be the  $z$ -axis, for example, then  $\mu = k_z/k$  where  $k = |\vec{k}|$ . In this paper the power spectrum in redshift space represents the average of  $P(k, \mu = k_x/k)$ ,  $P(k, \mu = k_y/k)$  and  $P(k, \mu = k_z/k)$  where the line of sight components are parallel to the  $x$ ,  $y$  and  $z$  directions respectively. We use this average as there is a significant scatter in the amplitudes of the three redshift space power spectra on large scales, even for a computational box as large as the one we have used. The three monopoles of the redshift space power spectra  $P(k, \mu = k_x/k)$ ,  $P(k, \mu = k_y/k)$  and  $P(k, \mu = k_z/k)$  measured in one of the realisations are plotted as the cyan, purple and red dashed lines respectively, to illustrate the scatter.

In Fig. 2 the Kaiser formula, given by Eq. 6, is plotted as a blue dotted line, using a value of  $f = \Omega_m^{0.55}(z)$  for  $\Lambda$ CDM. The error bars plotted represent the scatter over four realisations after averaging over  $P(k)$  obtained by treating the  $x, y$  and  $z$  directions as the line of sight. It is clear from this plot that the linear perturbation theory limit is only attained on extremely large scales ( $k < 0.03 h \text{Mpc}^{-1}$ ) at  $z = 0$  and at  $z = 1$ . Non-linear effects are significant on scales  $0.03 < k(h \text{Mpc}^{-1}) < 0.1$  which are usually considered to be in the linear regime. The measured variance in the matter power spectrum on these scales is  $10^{-3} < \sigma^2 < 10^{-2}$ .

In the right panel of Fig. 2 we plot the ratio  $P_2^s/P_0^s$  for  $\Lambda$ CDM at  $z = 0$  and  $z = 1$ . The ratio agrees with the Kaiser limit (given in Eq. 7) down to smaller scales,  $k < 0.06 h \text{Mpc}^{-1}$ , compared to the monopole ratio plotted in the left panel. Our results agree with previous work on the quadrupole and monopole moments of the redshift space power spectrum for  $\Lambda$ CDM (Cole et al. 1994; Hatton & Cole 1999; Scoccimarro 2004). At  $z = 1$ , the damping effects are less prominent and the Kaiser limit is attained over a slightly wider range of scales,  $k < 0.1 h \text{Mpc}^{-1}$ , as non-linear effects are smaller than at  $z = 0$ . In the next section, we consider these ratios for the quintessence dark energy models in more

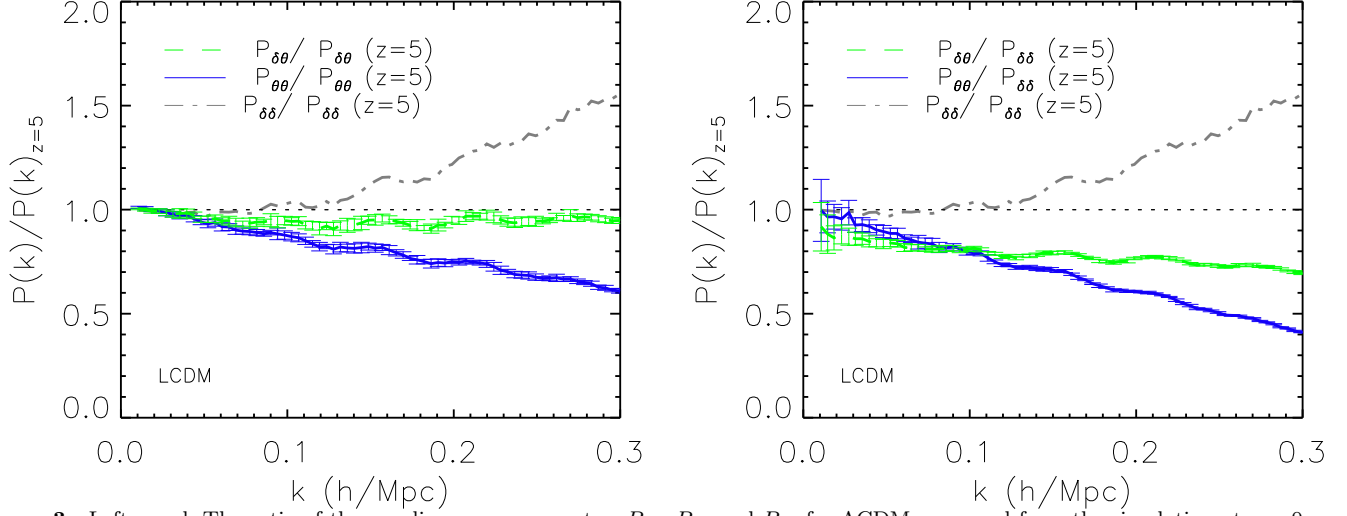


**Figure 3.** Left panel: The ratio of the non-linear power spectra,  $P_{\delta\delta}$ ,  $P_{\delta\theta}$  and  $P_{\theta\theta}$  for  $\Lambda$ CDM measured from the simulation at  $z = 0$ , divided by the corresponding power spectrum measured from the simulation at  $z = 5$ , scaled using the square of the ratio of the linear growth factor at  $z = 5$  and  $z = 0$ . The non-linear matter power spectrum is plotted as a grey dot-dashed line, the non-linear velocity divergence auto power spectrum  $P_{\theta\theta}$  is plotted as a blue solid line and the non-linear cross power spectrum,  $P_{\delta\theta}$ , is plotted as a green dashed line. Right panel: The ratio of the non-linear power spectra,  $P_{\delta\delta}$ ,  $P_{\delta\theta}$  and  $P_{\theta\theta}$ , to the linear theory matter  $P(k)$  in  $\Lambda$ CDM measured from the simulation at  $z = 0$ . All power spectra have been divided by the linear theory matter power spectrum measured from the simulation at  $z = 5$ , scaled using the square of the ratio of the linear growth factor at  $z = 5$  and  $z = 0$ . In both panels the error bars represent the scatter over eight  $\Lambda$ CDM realisations after imposing the peculiar velocity distortion along each cartesian axis in turn.

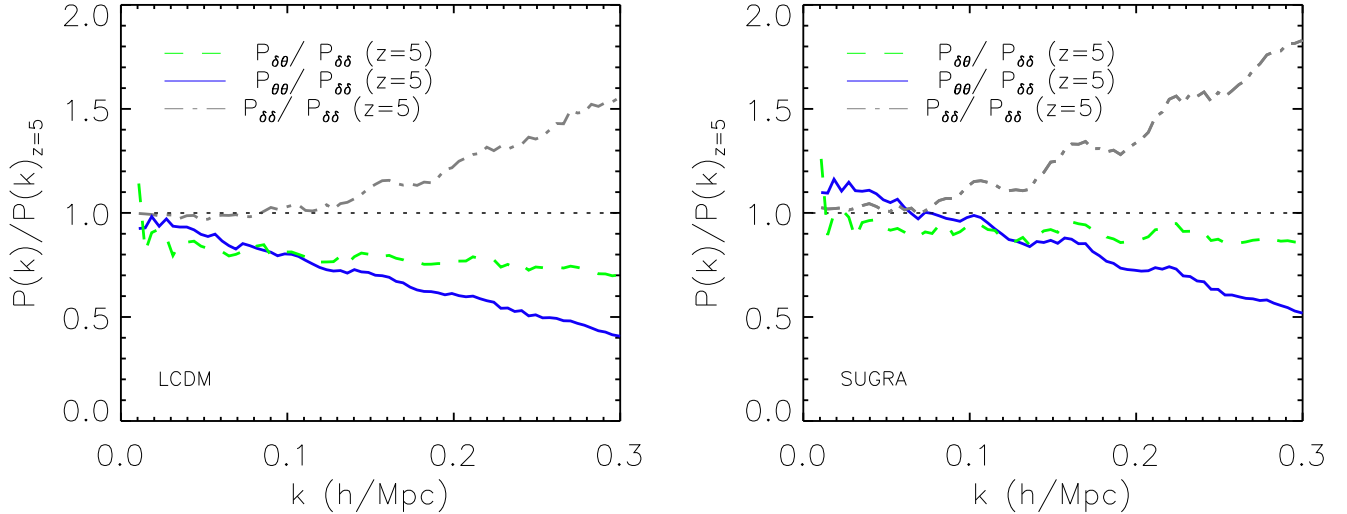


**Figure 4.** Left panel: The ratio of the non-linear power spectra,  $P_{\delta\delta}$ ,  $P_{\delta\theta}$  and  $P_{\theta\theta}$ , to the linear theory  $P(k)$  in  $\Lambda$ CDM measured from one realisation of the matter density and velocity fields at  $z = 0$ . All power spectra have been divided by the linear theory matter power spectrum measured from the simulation at  $z = 5$ , scaled using the square of the ratio of the linear growth factor at  $z = 5$  and  $z = 0$ . Right panel: Similar to that in the left panel but for the SUGRA quintessence model. The lines are the same as used in the left hand panel.

detail. For each model we find that the analytic expression for the quadrupole to monopole ratio describes the simulation results over a wider range of wavenumber than the analogous result for the monopole moment.

#### 4.2 Nonlinear models of $P_s(k, \mu)$

The linear theory relationship between the real and redshift space power spectra given in Eq. 6 assumes various non-linear effects are small and can be neglected on large scales. These assumptions are listed in Section 2.2. In this section

we consider the non-linear terms in the gradient of the line of sight velocity field and explore the scales at which it is correct to ignore such effects in the redshift space power spectrum. As a first step, we compare the model in Eq. 10, to measurements from N-body simulations for different quintessence dark energy models, without the damping term due to velocity dispersion. This will highlight the scale at which non-linear velocity divergence terms affect the matter power spectrum in redshift space and cause it to depart from the linear theory prediction.

If we rewrite  $d\delta/d\tau$  as  $aH(a)f(\Omega_m(a), \gamma)\delta$ , where  $\delta$  is



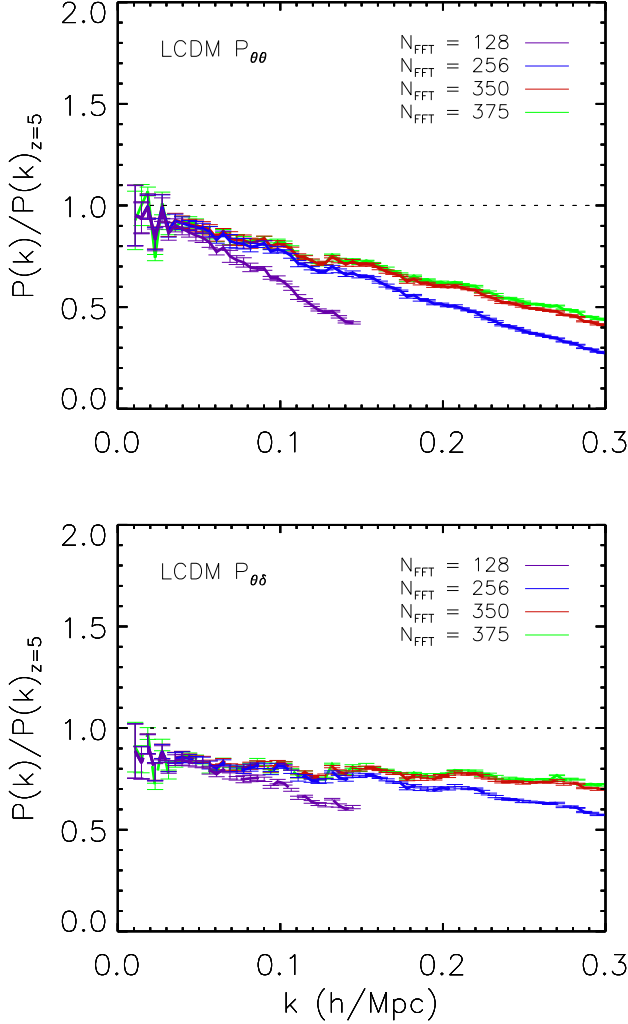


**Figure 5.** A comparison of the impact of the FFT grid dimension on power spectrum estimation. The plots show the ratio of the non-linear power spectra,  $P_{\theta\theta}$  (upper panel) and  $P_{\delta\delta}$  (lower panel), to the linear theory matter power spectrum measured from the simulations in  $\Lambda$ CDM, using different FFT grid sizes. From bottom to top in each panel the lines show the ratios for grid sizes  $N_{\text{FFT}} = 128$  (purple),  $N_{\text{FFT}} = 256$  (blue),  $N_{\text{FFT}} = 350$  (red) and  $N_{\text{FFT}} = 375$  (green).

the matter perturbation and  $\tau$  is the conformal time,  $dt = a(\tau)d\tau$ , then the linear continuity equation becomes

$$\theta = \vec{\nabla} \cdot \vec{u} = -aHf\delta. \quad (12)$$

Throughout this paper we normalise the velocity divergence as  $\theta(k, a)/[-aH(a)f(\Omega_m(a), \gamma)]$ , so  $\theta = \delta$  in the linear regime. The volume weighted velocity divergence power spectrum is calculated from the simulations according to the prescription given in Scoccimarro (2004). We interpolate the velocities and the densities onto a grid of  $350^3$  points and then measure the ratio of the interpolated momentum to the interpolated density field. In this way, we avoid having to correct for the CIC assignment scheme. A larger grid dimension could result in empty cells where  $\delta \rightarrow 0$ . A FFT grid of  $350^3$  was used to ensure all grid points had non-zero density and hence a well defined velocity at each point. We only plot the velocity power spectra in each of the fig-

ures up to half the Nyquist frequency for our default choice of  $N_{\text{FFT}} = 350^3$ ,  $k_{\text{Nyq}}/2 = \pi N_{\text{FFT}}/(2L_{\text{box}}) = 0.37h\text{Mpc}^{-1}$  which is beyond the range typically used in BAO fitting when assuming linear theory.

The left panel in Fig. 3 shows the ratio of the power spectra,  $P_{\delta\delta}$ ,  $P_{\delta\theta}$  and  $P_{\theta\theta}$  measured at  $z = 0$ , to the power spectra measured at  $z = 5$  scaled using the ratio of the square of the linear growth factor at  $z = 5$  and  $z = 0$  for  $\Lambda$ CDM. It is clear from this plot that all  $P(k)$  evolve as expected in linear theory on the largest scales. Note a linear scale is used on the  $x$ -axis in this case. In the right panel in Fig. 3 all the power spectra have been divided by the linear theory matter power spectrum measured from the simulation at  $z = 5$ , scaled using the ratio of the linear growth factor at  $z = 5$  and  $z = 0$ . This removes the sampling variance from the plotted ratio (Baugh & Efstathiou 1994). In both panels, the error bars represent the scatter over eight simulations in  $\Lambda$ CDM averaging the power spectra after imposing the distortions along the  $x$ ,  $y$  or  $z$  axis in turn. From this figure we can see that the non-linear velocity divergence power spectra can be substantially different from the matter power spectrum on very large scales  $k \sim 0.03h\text{Mpc}^{-1}$ . The linear perturbation theory assumption that the velocity divergence power spectra is the same as the matter  $P(k)$  is not valid even on these large scales. In the case of  $\Lambda$ CDM this difference is  $\sim 20\%$  at  $k = 0.1h\text{Mpc}^{-1}$ . Note in the right panel in Fig. 3, the 10% difference in the ratio of the cross power spectrum to the matter power spectrum, on the largest scale considered, indicates that we have a biased estimator of  $\theta$  which is low by approximately 10%.

We find that the  $P_{\delta\theta}$  and  $P_{\theta\theta}$  measured directly from the simulation differ from the matter power spectrum by more than was reported by Percival & White (2009). These authors did not measure  $P_{\delta\theta}$  and  $P_{\theta\theta}$  directly, but instead obtained these quantities by fitting Eq. 13 to the redshift space monopole power spectrum measured from the simulations. In Fig. 4 we plot the same ratios as shown in the right panel of Fig. 3 measured from one  $\Lambda$ CDM (left panel) and SUGRA (right panel) simulation. From our simulations it is possible to find a realisation of the density and velocity fields where the measured matter power spectrum and the velocity divergence power spectra are similar on large scales.

Having found that the measured  $P_{\delta\theta}$  and  $P_{\theta\theta}$  differ significantly from  $P_{\delta\delta}$ , we now test if the grid assignment scheme has any impact on our results. As explained in Section 4.2, the velocity  $P(k)$  are computed by taking the Fourier transform of the momentum field divided by the density field to reduce the impact of the grid assignment scheme (Scoccimarro 2004). Pueblas & Scoccimarro (2009) showed that the CIC assignment scheme affects the measured  $P(k)$  beyond  $\sim 20\%$  of the Nyquist frequency. In Fig. 5 we show the power spectrum measurements for four different FFT dimensions to show the scales at which we get a robust measurement. For  $N_{\text{FFT}} = 350$  the power spectra have converged on scales up to  $k \sim 0.2h\text{Mpc}^{-1}$ .

In the top row of Fig. 6, the ratios  $P_0^s(k)/P^r(k)$  and  $P_2^s(k)/P_0^s(k)$  are plotted as solid lines in the left and right hand panels respectively. In this figure we have overplotted as grey dashed lines, the ratio of the redshift space monopole



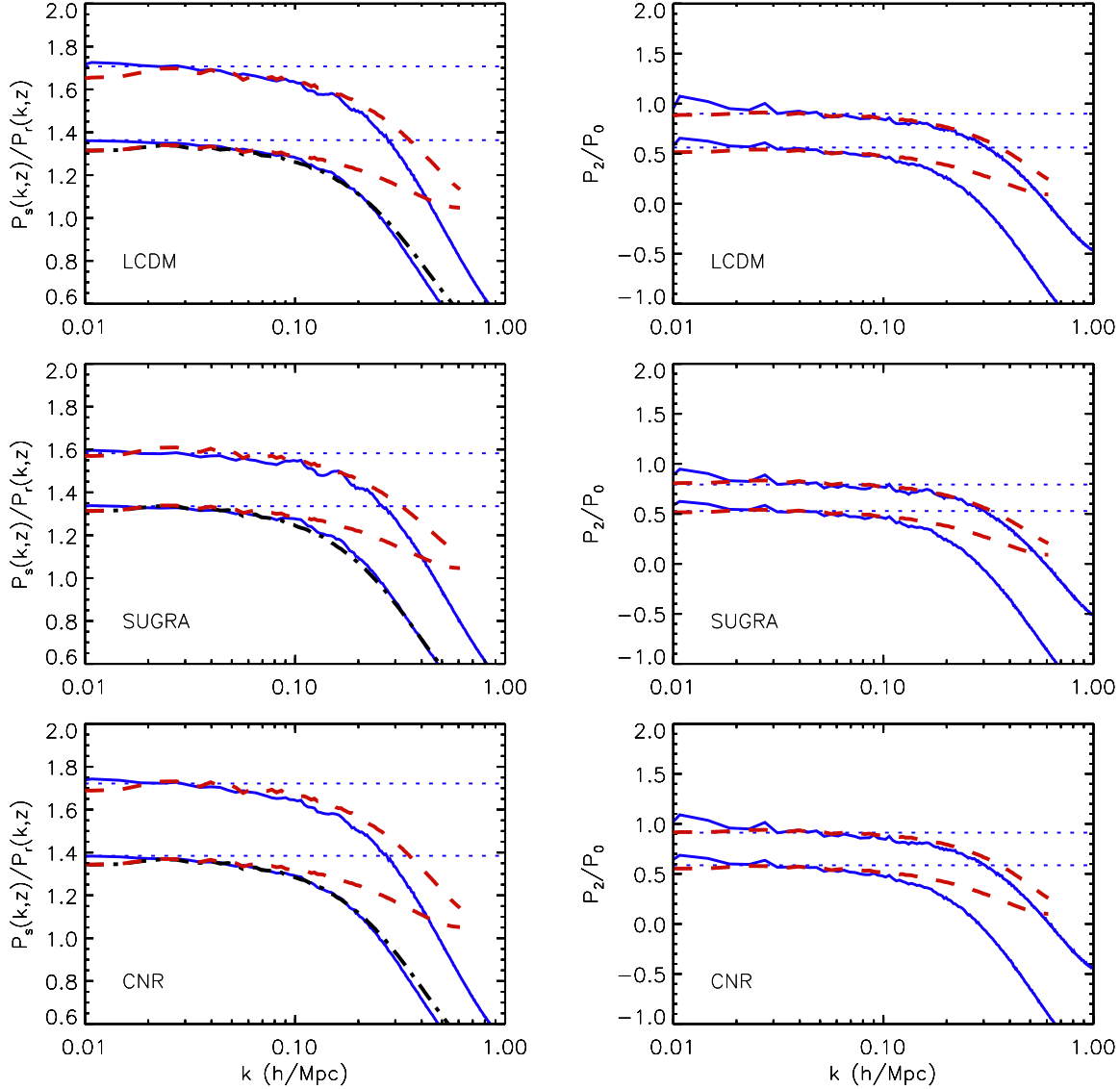


**Figure 6.** The left hand column shows the ratio of the monopole of redshift power spectra to the real space power spectra at  $z = 0$  and  $z = 1$ . The right hand column shows the ratio of the quadrupole to monopole moment of the redshift space power spectra at  $z = 0$  and  $z = 1$ . Different rows show different dark energy models as labelled. Top row: The ratio of the redshift and real space power spectra in  $\Lambda$ CDM are plotted as solid lines in the left panel. The dashed lines represent the same ratio using Eq. 13 for the monopole of the redshift space power spectrum. The dot-dash line represents the model given in Eq. 10 which includes velocity dispersion effects. In the right panel the ratio of the quadrupole to monopole moment of the redshift space power spectra in  $\Lambda$ CDM are plotted as solid lines. The same ratio using Eq. 14 for the redshift space power spectrum is plotted as dashed lines. Middle row: Same as the top row but for the SUGRA quintessence model. Bottom row: Same as the middle row but for the CNR quintessence model.

moment to the real space power spectrum where

$$P_0^s(k) = P_{\delta\delta}(k) + \frac{2}{3}fP_{\delta\theta}(k) + \frac{1}{5}f^2P_{\theta\theta}(k). \quad (13)$$

On scales  $0.05 < k(h\text{Mpc}^{-1}) < 0.2$ , this model for the redshift space power spectrum reproduces the measured  $P_s(k, \mu)$  and is a significant improvement compared to Eq. 6. This form does not include any modelling of the damping due to velocity dispersion. The extended model proposed by Scoccimarro (2004) given in Eq. 10, which does include damping, is also plotted as a black dot-dashed line for  $\Lambda$ CDM in the top row in Fig. 6. The redshift space quadrupole to monopole ratio in the quasi-linear regime,

including the velocity divergence power spectra, is

$$\frac{P_2^s}{P_0^s} = \frac{\frac{4}{3}fP_{\delta\theta} + \frac{4}{7}f^2P_{\theta\theta}}{P_{\delta\delta} + \frac{2}{3}fP_{\delta\theta} + \frac{1}{5}f^2P_{\theta\theta}}. \quad (14)$$

This model does well at reproducing the ratio of the redshift space to real space power spectrum, although it underpredicts the ratio on scales  $k < 0.02h\text{Mpc}^{-1}$ . The corresponding plots for the SUGRA and CNR models are shown in the middle and bottom rows of Fig. 6. It is clear that including the velocity divergence power spectrum in the model for  $P_0^s$  and  $P_2^s$ , produces a good fit to the measured redshift space power in both quintessence models on scales up to  $k \sim 0.2h\text{Mpc}^{-1}$ .

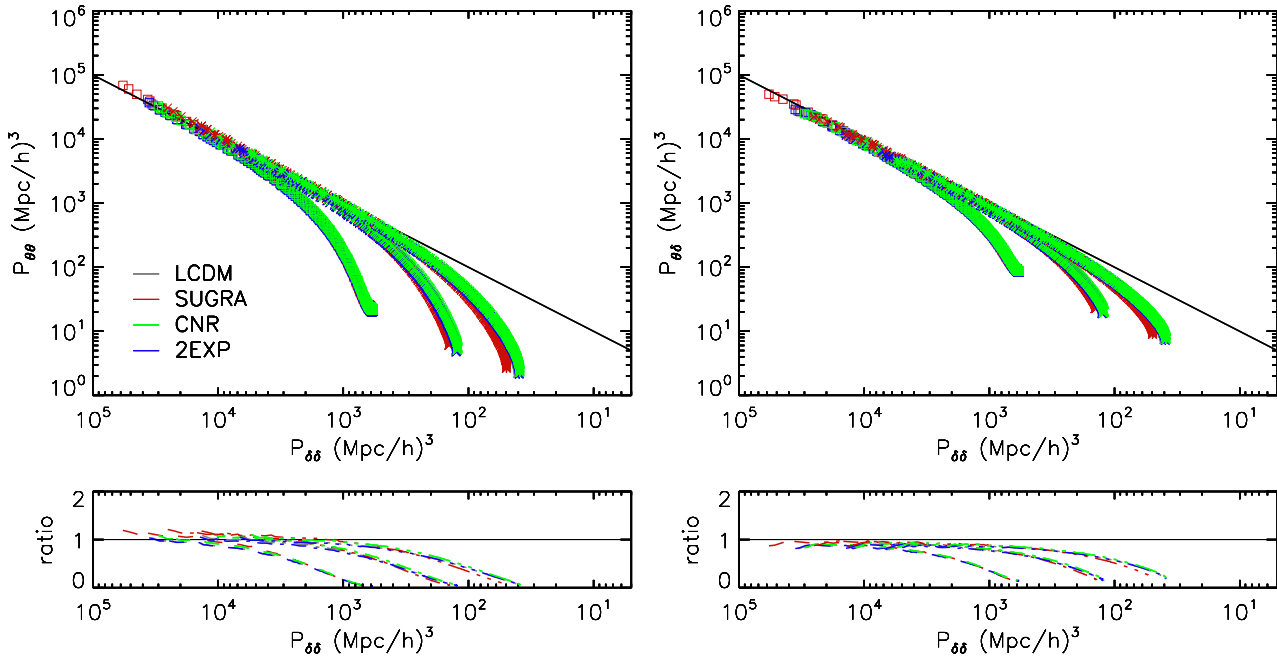


**Figure 7.** Non-linear velocity divergence auto (left) and cross (right) power spectrum plotted as a function of the non-linear matter power spectrum at  $z = 0, 1$  and  $2$  in three quintessence models and  $\Lambda$ CDM, as labelled. The ratio of the velocity divergence power spectra to the matter power spectrum at each redshift is plotted in the smaller panels beneath each main panel.

## 5 RESULTS II: THE DENSITY VELOCITY RELATION

In Section 5.1 we examine the relationship between the non-linear matter and velocity divergence power spectra in different cosmologies. In Section 5.2 we study the redshift dependence of this relationship and provide a prescription which can be followed to generate predictions for the non-linear velocity divergence power spectrum at a given redshift.

### 5.1 Dependence on cosmological model

The linear continuity equation, Eq. 12, gives a one to one correspondence between the velocity and density fields with a cosmology dependent factor,  $f(\Omega_m, \gamma)$ . Once the overdensities become non-linear, this relationship no longer holds. Bernardeau (1992) derived the non-linear relation between  $\delta$  and  $\theta$  in the case of an initially Gaussian field. Chodorowski & Lokas (1997) extended this relation into the weakly non-linear regime up to third order in perturbation theory and found the result to be a third order polynomial in  $\theta$ . More recently, Bilicki & Chodorowski (2008) found a relation between  $\theta$  and  $\delta$  using the spherical collapse model. In all of these relations, the dependence on cosmological parameters was found to be extremely weak (Bernardeau 1992; Bouchet et al. 1995). The velocity divergence depends on  $\Omega_m$  and  $\Omega_\Lambda$ , in a standard  $\Lambda$ CDM cosmology, only through the linear growth rate,  $f$  (Scoccimarro et al. 1999).

We showed in the previous section that including the velocity divergence auto and cross power spectrum accurately reproduces the redshift space power spectrum for a range of dark energy models on scales where the Kaiser formula fails. The quantities in Eqs. 14 and 10 can be calculated if we exploit the relationship between the velocity and density field. In Fig. 7 we plot the velocity divergence

auto (left panel) and cross (right panel) power spectrum as a function of the matter power spectrum for  $\Lambda$ CDM and the three quintessence dark energy models. We find that the density velocity relationship is very similar for each model at the redshifts considered, with only a slight difference for the SUGRA model at high redshifts and at small scales. The departure of the SUGRA model from the general density velocity relation is due to shot noise, which affects the power spectrum most at these scales in the SUGRA model as it has the lowest amplitude. We have verified that this effect is due to shot noise by sampling half the particles in the same volume, thereby doubling the shot noise, and repeating the  $P(k)$  measurement to find an even larger departure. Fig. 7 shows the independence of the density velocity relation not only of the values of cosmological parameters, as found in previous works, Bernardeau (1992), but also a lack of dependence on the cosmological expansion history and initial power spectrum.

Fitting over the range  $0.01 < k(h/\text{Mpc}) < 0.3$ , we find the following function accurately describes the relation between the non-linear velocity divergence and matter power spectrum at  $z = 0$  to better than 5% on scales  $k < 0.3h\text{Mpc}^{-1}$ ,

$$P_{xy}(k) = g(P_{\delta\delta}(k)) = \frac{\alpha_0 \sqrt{P_{\delta\delta}(k)} + \alpha_1 P_{\delta\delta}^2(k)}{\alpha_2 + \alpha_3 P_{\delta\delta}(k)}, \quad (15)$$

where  $P_{\delta\delta}$  is the non-linear matter power spectrum. For the cross power spectrum  $P_{xy} = P_{\delta\theta}$ ,  $\alpha_0 = -12288.7$ ,  $\alpha_1 = 1.43$ ,  $\alpha_2 = 1367.7$  and  $\alpha_3 = 1.54$  and for  $P_{xy} = P_{\theta\theta}$ ,  $\alpha_0 = -12462.1$ ,  $\alpha_1 = 0.839$ ,  $\alpha_2 = 1446.6$  and  $\alpha_3 = 0.806$ ; all points were weighted equally in the fit and the units for  $\alpha_0, \alpha_1$  and  $\alpha_3$  are  $(\text{Mpc}/h)^{3/2}$ ,  $(\text{Mpc}/h)^{-3}$  and  $(\text{Mpc}/h)^{-3}$  respectively. The power spectra used for this fit are the av-

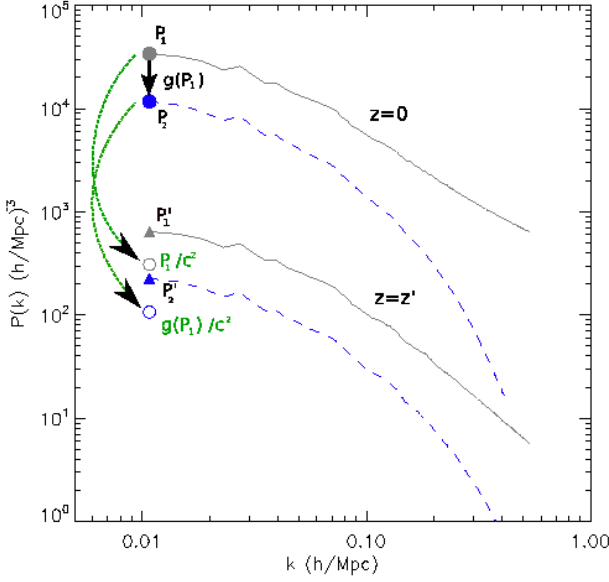


**Figure 8.** A schematic illustration showing how the  $z = 0$  non-linear matter power spectrum can be rescaled to find the velocity divergence power spectrum at any redshift  $z = z'$ . The upper two curves represent the non-linear matter power spectrum,  $P_1$ , in grey and the velocity divergence power spectrum,  $P_2$ , plotted as a blue dashed line, at  $z = 0$ . The power in the first bin is represented as a filled circle for each spectrum. The lower two curves,  $P_1'$  and  $P_2'$ , are the non-linear matter and velocity divergence spectra at  $z = z'$ . The power in the first bin is represented as a filled triangle in each case. The fitting formula for  $g(P_1)$  (Eq. 15) generates the non-linear velocity divergence power spectra at  $z = 0$ . Using the function given in Eq. 17, the matter power spectrum  $P_1$  and  $g(P_1)$  can be rescaled to an earlier redshift. The power in the first bin from the rescaled  $P_1$  and  $g(P_1)$  are shown as an empty grey and blue circle respectively. Note that  $P_1$  and  $P_2$  have been artificially separated for clarity.

erage  $P_{\theta\theta}$ ,  $P_{\delta\theta}$  and  $P_{\delta\delta}$  measured from eight  $\Lambda$ CDM simulations.

## 5.2 Approximate formula for $P_{\delta\theta}$ and $P_{\theta\theta}$ for arbitrary redshift

In perturbation theory, the solution for the density contrast is expanded as a series around the background value. Scoccimarro et al. (1998) found the following solutions for  $\delta$  and  $\theta$  to arbitrary order in perturbation theory,

$$\begin{aligned}\delta(k, \tau) &= \sum_{n=1}^{\infty} D_n(\tau) \delta_n(k) \\ \theta(k, \tau) &= \sum_{n=1}^{\infty} E_n(\tau) \theta_n(k),\end{aligned}\quad (16)$$

where  $\delta_1(k)$  and  $\theta_1(k)$  are linear in the initial density field,  $\delta_2$  and  $\theta_2$  are quadratic in the initial density field etc. Scoccimarro et al. (1998) showed that using a simple approximation to the equations of motion,  $f(\Omega_m) = \Omega_m^{1/2}$ , the equations become separable and  $E_n(\tau) = D_n(\tau) = D(\tau)^n$ , where  $D(\tau)$  is the linear growth factor of density perturbations. We shall use these solutions for  $\delta(k, \tau)$  and  $\theta(k, \tau)$  to approximate the redshift dependence of the density velocity relation found in Section 5.1. This relation does not depend

on the cosmological model but we shall assume a  $\Lambda$ CDM cosmology and find the approximate redshift dependence as a function of the  $\Lambda$ CDM linear growth factor.

The fitting function given in Eq. 15 generates the non-linear velocity divergence power spectrum,  $P_{\delta\theta}$  or  $P_{\theta\theta}$  from the non-linear matter power spectrum,  $P_{\delta\delta}$  at  $z = 0$ . Fig. 8 shows a simple illustration of how the function  $g(P_{\delta\delta})$  and  $P_{\delta\delta}$  at  $z = 0$  can be rescaled to give the velocity divergence power spectra at a higher redshift,  $z'$ . Using the simplified notation in the diagram, where  $P_1 = P_{\delta\delta}$ , and given the function  $g(P_{\delta\delta})$ , we can find a redshift dependent function,  $c(z)$ , with which to rescale  $g(P_{\delta\delta}(z = 0))$  to the velocity divergence  $P(k)$  at  $z'$ . At the higher redshift,  $z'$ , the non-linear matter and velocity divergence power spectra are denoted as  $P_1'$  and  $P_2'$  respectively in Fig. 8.

Using the solutions in Eq. 16, to third order in perturbation theory, see Appendix A, we assume a simple expansion with respect to the initial density field, to find the following ansatz for the mapping  $P_1'(z = z') \rightarrow P_2'(z = z')$  which can be approximated as  $P_1(z = 0)/c^2(z = 0, z') \rightarrow g(P_1)/c^2(z = 0, z')$  where

$$c(z, z') = \frac{D(z) + D^2(z) + D^3(z)}{D(z') + D^2(z') + D^3(z')}, \quad (17)$$

and  $D(z)$  is the linear growth factor. The equivalence of these mappings gives  $P_1' - P_2' = (P_1 - g(P_1))/c^2$  which allows us to calculate  $P_2'$  at  $z = z'$  if we have  $P_1(z = 0)$ ,  $g(P_1(z = 0))$  and  $P_1'(z = z')$ . Writing this now in terms of  $P_{\delta\delta}$ , instead of  $P_1$ , we have the following equation

$$P_{xy}(k, z') = \frac{g(P_{\delta\delta}(k, z = 0)) - P_{\delta\delta}(k, z = 0)}{c^2(z = 0, z')} + P_{\delta\delta}(k, z'), \quad (18)$$

where  $g(P_{\delta\delta})$  is the function in Eq. 15 and  $P_{xy}$  is either the nonlinear cross or auto power spectrum,  $P_{\delta\theta}$  or  $P_{\theta\delta}$ .

In the left panel of Fig. 9, we plot the  $\Lambda$ CDM non-linear power spectrum  $P_{\theta\theta}$  at  $z = 0, 1, 2$  and  $3$ . The function given in Eq. 18 is also plotted as red dashed lines using the factor  $c(z, z')$  given in Eq. 17 and the  $\Lambda$ CDM linear growth factor at redshift  $z = 0, 1, 2$  and  $3$  respectively. The ratio plot shows the difference between the exact  $P_{\theta\theta}$  power spectrum and the function given in Eq. 18. The right panel in Fig. 9 shows a similar plot for the  $P_{\delta\theta}$  power spectrum. In both cases we find very good agreement between the scaled fitting formula and the measured power spectrum. Scaling the  $z = 0$  power spectra using this approximation in Eq. 17 reproduces the non-linear  $z = 1, 2$  and  $3$ ,  $P_{\delta\theta}$  to  $\sim 5\%$  and  $P_{\theta\theta}$  to better than  $5\%$  on scales  $0.05 < k(h\text{Mpc}^{-1}) < 0.2$ . It is remarkable that scaling the  $z = 0$  fitting formula using  $c$  in Eq. 17 works so well at the different redshifts up to  $k < 0.3h/\text{Mpc}$  and is completely independent of scale.

To summarise the results of this section we have found that the quadrupole to monopole ratio given in Eq. 14 and the model in Eq. 10, which includes the non-linear matter and velocity divergence power spectra at a given redshift  $z'$ , can be simplified by using the following prescription. Assuming a cosmology with a given linear theory matter power spectrum we can compute the non-linear matter  $P(k)$  at  $z=0$  and at the required redshift,  $z'$ , using, for example, the phenomenological model HALOFIT (Smith et al. 2003) or the method proposed by Casarini et al. (2009) in the case of quintessence dark energy. These power spectra can then be

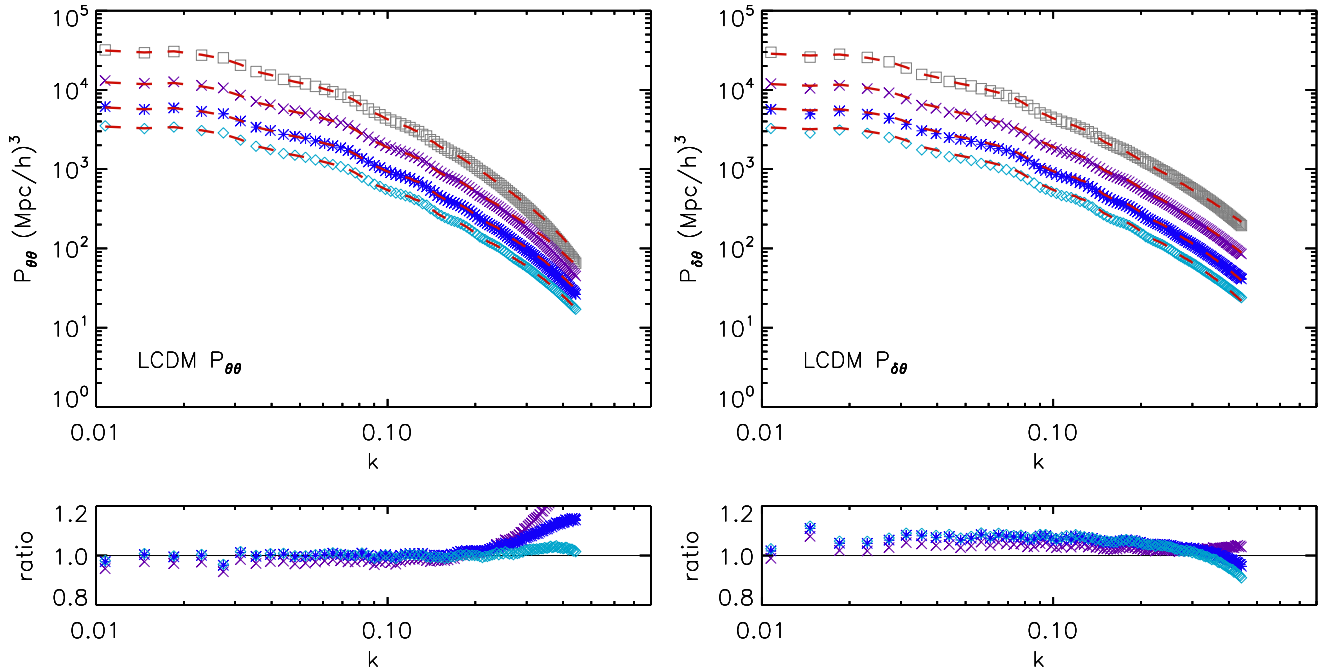


**Figure 9.** Non-linear velocity divergence auto and cross power spectrum, in the left and right panels respectively, measured from the  $\Lambda$ CDM simulations at  $z = 0$  (open grey squares),  $z = 1$  (purple crosses),  $z = 2$  (blue stars) and  $z = 3$  (cyan diamonds). Overplotted as red dashed lines is the function given in Eq. 18 at redshifts  $z = 1, 2$  and  $3$ . The lower panels show the function in Eq. 18 divided by the measured spectra at  $z = 1, 2$  and  $3$ .

used in Eq. 18 together with the function  $g$ , given in Eq. 15, and the linear theory growth factor between redshift  $z = 0$  and  $z = z'$  to find the velocity divergence auto or cross power spectrum. As can be seen from Fig. 9 the function given in Eq. 18 agrees with the measured non-linear velocity divergence power spectrum to  $\sim 10\%$  for  $k < 0.3h\text{Mpc}^{-1}$  and to  $< 5\%$  for  $k < 0.2h\text{Mpc}^{-1}$  for  $\Lambda$ CDM. We have verified that this prescription also reproduces  $P_{\delta\theta}$  and  $P_{\theta\theta}$  to an accuracy of  $10\%$  for  $k < 0.3h\text{Mpc}^{-1}$  for the CNR, SUGRA and 2EXP models using the corresponding matter power spectrum and linear growth factor for each model. This procedure simplifies the redshift space power spectrum in Eq. 10 and the quadrupole to monopole ratio given in Eq. 14. For the dark energy models considered in this paper, this ratio provides an improved fit to the redshift space  $P(k, \mu)$  compared to the Kaiser formula and incorporating the density velocity relation eliminates any new parameters which need to be measured separately and may depend on the cosmological model.

## 6 CONCLUSIONS AND SUMMARY

One of the primary goals of future galaxy redshift surveys is to determine the physics behind the accelerating expansion of the Universe by making an accurate measurement of the growth rate,  $f$ , of large scale structure (Cimatti et al. 2009). Measuring the growth rate with an error of less than  $10\%$  is one of the main science goals of Euclid, as this will allow us to distinguish modified gravity from dark energy models. With an independent measurement of the expansion history, the predicted growth rate for a dark energy model would agree with the observed value of  $f$  if general relativity holds.

We use simulations of three quintessence dark energy models which have different expansion histories, linear growth rates and power spectra compared to  $\Lambda$ CDM. In a previous paper, Jennings et al. (2010), we carried out the first fully consistent N-body simulations of quintessence dark energy, taking into account different expansion histories, linear theory power spectra and best fitting cosmological parameters  $\Omega_m$ ,  $\Omega_b$  and  $H_0$ , for each model. In this paper we examine the redshift space distortions in the SUGRA, CNR and 2EXP quintessence models. These models are representative of a broader class of quintessence models which have different growth histories and dark energy densities at early times compared to  $\Lambda$ CDM. In particular the SUGRA model has a linear growth rate that differs from  $\Lambda$ CDM by  $\sim 20\%$  at  $z = 5$  and the CNR model has high levels of dark energy at early times,  $\Omega_{DE} \sim 0.03$  at  $z \sim 200$ . The 2EXP model has a similar expansion history to  $\Lambda$ CDM at low redshifts,  $z < 5$ , despite having a dynamical equation of state for the dark energy component. For more details on each of the dark energy models see Jennings et al. (2010).

Redshift space distortions observed in galaxy surveys are the result of peculiar velocities which are coherent on large scales, leading to a boost in the observed redshift space power spectrum compared to the real space power spectrum (Kaiser 1987). On small scales these peculiar velocities are incoherent and give rise to a damping in the ratio of the redshift to real space power spectrum. The Kaiser formula is a prediction of the boost in this ratio on very large scales, where the growth is assumed to be linear, and can be expressed as a function of the linear growth rate and bias, neglecting all non-linear contributions.

In previous work, using N-body simulations in a periodic cube of  $300h^{-1}\text{Mpc}$  on a side, Cole et al. (1994)

found that the measured value of  $\beta = f/b$ , where  $b$  is the linear bias, deviates from the Kaiser formula on wavelengths of  $50h^{-1}$  Mpc or more as a result of these non-linearities. Hatton & Cole (1998) extended this analysis to slightly larger scales using the Zel'dovich approximation combined with a dispersion model where non-linear velocities are treated as random perturbations to the linear theory velocity. These previous studies do not provide an accurate description of the non-linearities in the velocity field for two reasons. Firstly, the Zel'dovich approximation does not model the velocities correctly, as it only treats part of the bulk motions. Secondly, in a computational box of length  $300h^{-1}$  Mpc, the power which determines the bulk flows has not converged. In this work we use a large computational box of side  $1500h^{-1}$  Mpc, which allows us to measure redshift space distortions on large scales to far greater accuracy than in previous work.

In this paper we find that the ratio of the monopole of the redshift space power spectrum to the real space power spectrum agrees with the linear theory Kaiser formula only on extremely large scales  $k < 0.03h\text{Mpc}^{-1}$  in both  $\Lambda$ CDM and the quintessence dark energy models. We still find significant scatter between choosing different axes as the line of sight, even though we have used a much larger simulation box than that employed in previous studies. As a result we average over the three power spectra, assuming the distortions lie along the  $x$ ,  $y$  and  $z$  directions in turn, for the redshift space power spectrum in this paper. Instead of using the measured matter power spectrum in real space, we find that the estimator suggested by Cole et al. (1994), involving the ratio of the quadrupole to monopole redshift space power spectrum, works better than using the monopole and agrees with the expected linear theory on slightly smaller scales  $k < 0.07h\text{Mpc}^{-1}$  at  $z = 0$  for both  $\Lambda$ CDM and the quintessence models.

As the measured redshift space distortions only agree with the Kaiser formula on scales  $k < 0.07h\text{Mpc}^{-1}$ , it is clear that the linear approximation is not correct on scales which are normally considered to be in the 'linear regime',  $k < 0.2h\text{Mpc}^{-1}$ . In linear theory, the velocity divergence power spectrum is simply a product of the matter power spectrum and the square of the linear growth rate. In this work we have demonstrated that non-linear terms in the velocity divergence power spectrum persist on scales  $0.04 < k(h\text{Mpc}^{-1}) < 0.2$ . These results agree with Scoccimarro (2004) who also found significant non-linear corrections due to the evolution of the velocity fields on large scales, assuming a  $\Lambda$ CDM cosmology. We have shown that including the non-linear velocity divergence auto and cross power spectrum in the expression for the redshift space  $P(k)$  leads to a significant improvement when trying to match the measured quadrupole to monopole ratio for both  $\Lambda$ CDM and quintessence dark energy models.

Including the non-linear velocity divergence cross and auto power spectra in the expression for the redshift space power spectrum increases the number of parameters needed and depends on the cosmological model that is used. Using the non-linear matter and velocity divergence power spectra we have found a density velocity relation which is model independent over a range of redshifts. Using this relation it is possible to write the non-linear velocity divergence auto or cross power spectrum at a given redshift,  $z'$ , in terms

of the non-linear matter power spectrum and linear growth factor at  $z = 0$  and  $z = z'$ . This formula is given in Eq. 18 in Section 5.2. We find that this formula accurately reproduces the non-linear velocity divergence  $P(k)$  to within 10% for  $k < 0.3h\text{Mpc}^{-1}$  and to better than 5% for  $k < 0.2h\text{Mpc}^{-1}$  for both  $\Lambda$ CDM and the dark energy models used in this paper.

It is clear that including the non-linear velocity divergence terms results in an improved model for redshift space distortions on scales  $k < 0.2h\text{Mpc}^{-1}$  for different cosmological models. Current galaxy redshift surveys can provide only very weak constraints on  $P_{\delta\theta}$  and  $P_{\theta\theta}$  (Tegmark et al. 2002). The relation given in this paper between the non-linear velocity divergence and matter power spectra will be useful for analysing redshift space distortions in future galaxy surveys as it removes the need to use noisier and sparser velocity data.

## ACKNOWLEDGMENTS

EJ acknowledges receipt of a fellowship funded by the European Commission's Framework Programme 6, through the Marie Curie Early Stage Training project MEST-CT-2005-021074. This work was supported in part by grants from the Science and Technology Facilities Council held by the ICC and the Institute for Particle Physics Phenomenology at Durham University. We acknowledge helpful conversations with Shaun Cole and Martin Crocce.

## REFERENCES

- Barreiro T., Copeland E. J., Nunes N. J., 2000, Phys. Rev. D, 61, 127301
- Baugh C. M., Efstathiou G., 1994, MNRAS, 270, 183
- Baugh C. M., Gaztanaga E., Efstathiou G., 1995, MNRAS, 274, 1049
- Baumgart D. J., Fry J. N., 1991, ApJ, 375, 25
- Bernardeau F., 1992, ApJ, 390, L61
- Bernardeau F., Colombi S., Gaztanaga E., Scoccimarro R., 2002, Phys. Rept., 367, 1
- Bilicki M., Chodorowski M. J., 2008, MNRAS, 391, 1796
- Bouchet F. R., Colombi S., Hivon E., Juszkiewicz R., 1995, Astron. Astrophys., 296, 575
- Brax P., Martin J., 1999, Phys. Lett., B468, 40
- Caldwell R. R., Dave R., Steinhardt P. J., 1998, PhRvL, 80, 1582
- Casarini L., Macciò A. V., Bonometto S. A., 2009, JCAP, 3, 14
- Chodorowski M. J., Lokas E. L., 1997, MNRAS, 287, 591
- Cimatti A., et al., 2009, Experimental Astronomy, 23, 39
- Cole S., 1997, MNRAS, 286, 38
- Cole S., Fisher K. B., Weinberg D. H., 1994, MNRAS, 267, 785
- Copeland E. J., Nunes N. J., Rosati F., 2000, Phys. Rev. D, 62, 123503
- Copeland E. J., Sami M., Tsujikawa S., 2006, Int. J. Mod. Phys., D15, 1753
- Corasaniti P. S., Copeland E. J., 2003, Phys. Rev. D, 67, 063521
- Doran M., Robbers G., 2006, JCAP, 0606, 026

Dvali G. R., Gabadadze G., Porrati M., 2000, Phys. Lett., B485, 208

Fang W., Hu W., Lewis A., 2008, Phys. Rev. D, 78, 087303

Ferreira P. G., Joyce M., 1998, Phys. Rev. D, 58, 023503

Fisher K. B., 1995, ApJ, 448, 494

Guzzo L., et al., 2008, Nature, 451, 541

Hamilton A. J. S., 1998 Vol. 231 of Ap&SS. p. 185

Hatton S., Cole S., 1999, MNRAS, 310, 1137

Hatton S. J., Cole S., 1998, MNRAS, 296, 10

Hockney R. W., Eastwood J. W., 1981, Computer Simulation Using Particles

Jackson J., 1972, MNRAS, 156, 1P

Jennings E., Baugh C. M., Angulo R. E., Pascoli S., 2010, MNRAS, 401, 2181

Kaiser N., 1987, MNRAS, 227, 1

Komatsu E., et al., 2009, ApJS, 180, 330

Lahav O., Lilje P. B., Primack J. R., Rees M. J., 1991, MNRAS, 251, 128

Le Fevre O., et al., 2005, A&A, 439, 845

Lewis A., Bridle S., 2002, Phys. Rev. D, 66, 103511

Linder E. V., 2005, Phys. Rev. D, 72, 043529

Linder E. V., 2008, Astroparticle Physics, 29, 336

Linder E. V., 2009, Phys. Rev., 79, 063519

Linder E. V., Cahn R. N., 2007, Astropart. Phys., 28, 481

Lue A., Scoccimarro R., Starkman G. D., 2004, Phys. Rev. D, 69, 124015

Oyaizu H., 2008, Phys. Rev., 78, 123523

Peacock J. A., Dodds S. J., 1994, MNRAS, 267, 1020

Peacock J. A., et al., 2001, Nature, 410, 169

Peebles P. J. E., 1976, ApJ, 205, 318

Peebles P. J. E., 1980, The Large Scale Structure of the Universe

Percival W. J., White M., 2009, MNRAS, 393, 297

Pueblas S., Scoccimarro R., 2009, Phys. Rev. D, 80, 043504

Ratra B., Peebles P. J. E., 1988, Phys. Rev. D, 37, 3406

Sánchez A. G., Crocce M., Cabré A., Baugh C. M., Gaztañaga E., 2009, MNRAS, 400, 1643

Scoccimarro R., 2004, Phys. Rev. D, 70, 083007

Scoccimarro R., Couchman H. M. P., Frieman J. A., 1999, ApJ, 517, 531

Scoccimarro R., et al., 1998, ApJ, 496, 586

Simpson F., Peacock J. A., 2010, Phys. Rev. D, 81, 043512

Smith R. E., et al., 2003, MNRAS, 341, 1311

Song Y., Percival W. J., 2009, JCAP, 10, 4

Springel V., 2005, MNRAS, 364, 1105

Stril A., Cahn R. N., Linder E. V., 2010, MNRAS, 404, 239

Tegmark M., Hamilton A. J. S., Xu Y., 2002, MNRAS, 335, 887

Wang L.-M., Steinhardt P. J., 1998, ApJ, 508, 483

Wang Y., 2008, JCAP, 0805, 021

Wetterich C., 1988, Nucl. Phys. B, 302, 668

White M., Song Y., Percival W. J., 2009, MNRAS, 397, 1348

White S. D. M., 1994, RvMA, 7, 255

Yoshida N., Sheth R. K., Diaferio A., 2001, MNRAS, 328, 669

## APPENDIX A: APPROXIMATE FORMULA FOR $P_{\delta\theta}$ AND $P_{\theta\theta}$ FOR ARBITRARY REDSHIFT

Eq. 18 in this paper relates  $P_{xy}(z') - P_{\delta\delta}(z')$  at  $z = z'$  to the same expression at redshift  $z = 0$  using a variable  $c^2$ . Note from Eq. 15  $g(P_{\delta\delta}(z = 0)) = P_{xy}(z = 0)$  in Eq. 18. From Eqs. 16 in our paper and using the result by Scoccimarro et al. 1998 we can write the following solutions for  $\theta$  and  $\delta$  in terms of scalings of the initial density field (Bernardeau et al. 2002),

$$\theta(z) = D(z)\theta_1 + D^2(z)\theta_2 + D^3(z)\theta_3 + \dots \quad (\text{A1})$$

and

$$\delta(z) = D(z)\delta_1 + D^2(z)\delta_2 + D^3(z)\delta_3 + \dots \quad (\text{A2})$$

Squaring these expressions and ensemble averaging we can write the velocity divergence power spectrum and the matter power spectrum to third order in perturbation theory as

$$P_{\theta\theta}(z') \sim \langle |D(z')\theta_1 + D^2(z')\theta_2 + D^3(z')\theta_3|^2 \rangle \quad (\text{A3})$$

$$P_{\delta\delta}(z') \sim \langle |D(z')\delta_1 + D^2(z')\delta_2 + D^3(z')\delta_3|^2 \rangle \quad (\text{A4})$$

Using the fact that  $|D\theta_1 + D^2\theta_2 + D^3\theta_3| \leq |D\theta_1| + |D^2\theta_2| + |D^3\theta_3|$  we can approximate this as

$$P_{\theta\theta}(z') \leq \langle (D(z')|\theta_1| + D^2(z')|\theta_2| + D^3(z')|\theta_3|)^2 \rangle \quad (\text{A5})$$

$$P_{\delta\delta}(z') \leq \langle (D(z')|\delta_1| + D^2(z')|\delta_2| + D^3(z')|\delta_3|)^2 \rangle, \quad (\text{A6})$$

and we assume that

$$\langle |D(z')\theta_1 + D^2(z')\theta_2 + D^3(z')\theta_3|^2 \rangle \quad (\text{A7})$$

$$= \langle (D(z')|\theta_1| + D^2(z')|\theta_2| + D^3(z')|\theta_3|)^2 \rangle \sim$$

$$\langle |D(z')\delta_1 + D^2(z')\delta_2 + D^3(z')\delta_3|^2 \rangle$$

$$= \langle (D(z')|\delta_1| + D^2(z')|\delta_2| + D^3(z')|\delta_3|)^2 \rangle.$$

Taking the difference of the two power spectra we have

$$P_{\theta\theta}(z') - P_{\delta\delta}(z') \sim$$

$$\langle (D(z')|\theta_1| + D^2(z')|\theta_2| + D^3(z')|\theta_3|)^2 \rangle$$

$$- \langle (D(z')|\delta_1| + D^2(z')|\delta_2| + D^3(z')|\delta_3|)^2 \rangle \quad (\text{A8})$$

and as  $x^2 - y^2 = (x - y)(x + y)$  we can rewrite this as

$$P_{\theta\theta}(z') - P_{\delta\delta}(z') \sim \quad (\text{A9})$$

$$\langle [D(|\theta_1| - |\delta_1|) + D^2(|\theta_2| - |\delta_2|) + D^3(|\theta_3| - |\delta_3|)]$$

$$\times [D(|\theta_1| + |\delta_1|) + D^2(|\theta_2| + |\delta_2|) + D^3(|\theta_3| + |\delta_3|)] \rangle.$$

Multiplying out the rhs of this equation and denoting the modulus of variable  $|x|$  as  $x$  for simplicity, we have

$$P_{\theta\theta}(z') - P_{\delta\delta}(z') \sim \quad (\text{A10})$$

$$\begin{aligned} & \langle \{ D^2[\theta_1^2 - \delta_1^2] + D^3[(\theta_1 - \delta_1)(\theta_2 + \delta_2) + (\theta_1 + \delta_1)(\theta_2 - \delta_2)] \\ & + D^4[(\theta_1 - \delta_1)(\theta_3 + \delta_3) + (\theta_2^2 - \delta_2^2) + (\theta_1 + \delta_1)(\theta_3 - \delta_3)] \\ & + D^5[(\theta_2 - \delta_2)(\theta_3 + \delta_3) + (\theta_2 + \delta_2)(\theta_3 - \delta_3)] + D^6[\theta_3^2 - \delta_3^2] \} \rangle, \end{aligned}$$

and then taking out a factor of  $[\theta_1^2 - \delta_1^2]$  on the rhs we have

$$P_{\theta\theta}(z') - P_{\delta\delta}(z') \sim \quad (\text{A11})$$

$$\langle [\theta_1^2 - \delta_1^2] \{ D^2 + D^3 \left[ \frac{\theta_2 + \delta_2}{\theta_1 + \delta_1} + \frac{\theta_2 - \delta_2}{\theta_1 - \delta_1} \right]$$

$$+ D^4 \left[ \frac{\theta_3 + \delta_3}{\theta_1 + \delta_1} + \frac{\theta_2^2 - \delta_2^2}{\theta_1^2 - \delta_1^2} + \frac{\theta_3 - \delta_3}{\theta_1 - \delta_1} \right]$$

$$+ D^5 \left[ 2 \frac{\theta_3\theta_2 - \delta_3\delta_2}{\theta_1^2 - \delta_1^2} \right] + D^6 \left[ \frac{\theta_3^2 - \delta_3^2}{\theta_1^2 - \delta_1^2} \right] \} \rangle.$$

As  $\theta_1$  and  $\delta_1$  are linear in the initial density contrast, which we assume to be different to the linear density contrast,  $\theta_1 \sim \delta_1 \sim \delta_i$  and  $\theta_2 \sim \delta_2 \sim \delta_i + \delta_i^2$  is quadratic in the initial density contrast and  $\theta_3 \sim \delta_3 \sim \delta_i + \delta_i^2 + \delta_i^3$  is cubic in the initial density field, we assume  $\theta_1 + \theta_2 \sim \delta_1 + \delta_2$ ,  $\theta_1 + \theta_3 \sim \delta_1 + \delta_3$  and  $\theta_1 - \theta_2 \sim \delta_1 - \delta_2$ ,  $\theta_1 - \theta_3 \sim \delta_1 - \delta_3$  so the fractions in the above equation are unity and

$$\begin{aligned} P_{\theta\theta}(z') - P_{\delta\delta}(z') & \quad (A12) \\ \sim & \quad < [\theta_1^2 - \delta_1^2] > \{D^2 + 2D^3 + 3D^4 + 2D^5 + D^6\} \\ \sim & \quad < [\theta_1^2 - \delta_1^2] > \{D(z') + D^2(z') + D^3(z')\}^2 \end{aligned}$$

Similarly for  $P_{\theta\theta}(z) - P_{\delta\delta}(z)$  we have

$$\begin{aligned} P_{\theta\theta}(z) - P_{\delta\delta}(z) & \quad (A13) \\ \sim & \quad < [\theta_1^2 - \delta_1^2] > \{D(z) + D^2(z) + D^3(z)\}^2 \end{aligned}$$

Taking the ratio of the two previous equations, the redshift independent factor  $[\theta_1^2 - \delta_1^2]$  cancels and we obtain the following ansatz

$$\frac{P_{\theta\theta}(z') - P_{\delta\delta}(z')}{P_{\theta\theta}(z) - P_{\delta\delta}(z)} \sim \frac{[D(z') + D(z')^2 + D(z')^3]^2}{[D(z) + D(z)^2 + D(z)^3]^2} \quad (A14)$$

which is the expression in Eq. 18 in the paper for  $z = 0$ . A similar approximation works for the cross power spectrum  $P_{\delta\theta}$ .

This paper has been typeset from a  $\text{\LaTeX}$  file prepared by the author.